

Numerical Investigations of Transient Nozzle Flow Separation

By A. Chaudhuri†, A. Hadjadj‡ AND R. Friedrich¶

† Gyeongsang National University, Jinju, Gyeongnam 660-701, South Korea

‡ CORIA - INSA & University of Rouen, 76801 St Etienne du Rouvray, France

¶ Technische Universität München, 85747 Garching, Germany

Large-eddy simulations are carried out to investigate the shock induced transient flow through a planar nozzle mimicking a shock tube experimental setup with shock Mach number $M_s = 1.86$. Higher mesh resolution and larger spanwise domain size are chosen compared to the previous study in order to capture the flow separation and secondary shock boundary layer interaction observed in the experiment. A fifth-order Weighted Essentially Non-oscillatory (WENO) scheme based 3D numerical flow solver equipped with an immersed boundary method and Wall-Adapting Local Eddy-viscosity (WALE) model is used for this purpose. A homogeneous incompressible isotropic turbulence superimposed on the shocked section is assigned as initial fluctuating field. Results show substantial improvements in the prediction of the secondary shock, separation shock and flow separation compared to the previous findings dealt with lower mesh resolution and smaller spanwise dimension. The turbulent flow structures are depicted utilising the mean flow-field which is spatially averaged over the spanwise homogenous direction. Time-averaging on the fly turns out to be inadequate, since it leads to a spatial shift of the separation bubble. The reason for this is the use of past flow information only, due to the lack of future information. This, in-turn invokes the need of phase-averaging to extract stable and physically meaningful statistics of the turbulent flow-field for further deeper analysis.

1. Introduction

Control of flow separation in rocket nozzles is a challenging problem in aerospace science, not only for current engines confronted with problems of thermo-mechanical loads, but also for future engines which could work with very wide separation zones. This phenomenon is related to a usually unstable type of flow occurring in large expansion nozzles and thereby producing large side-loads. The shape of the nozzle (planar, conical or contoured) has an important influence on the type of flow separation (free- or restricted-shock separation). It is considered that for the parabolic nozzles, the transition of the flow structure from free shock separation (FSS) to restricted shock separation (RSS) and vice versa creates a sudden change in wall pressure, resulting in the generation of side-loads [1–7]. The physical problem met in those configurations is essentially due to the boundary layer separation during the nozzle startup process, caused by the ambient high pressure gradient, resulting in the complex phenomenon with shock/shock and shock/boundary layer interactions.

Only a few researchers have investigated transient nozzle flows during engine start-up. Experimental investigations have been performed by Smith [8], Amann [9], Saito et

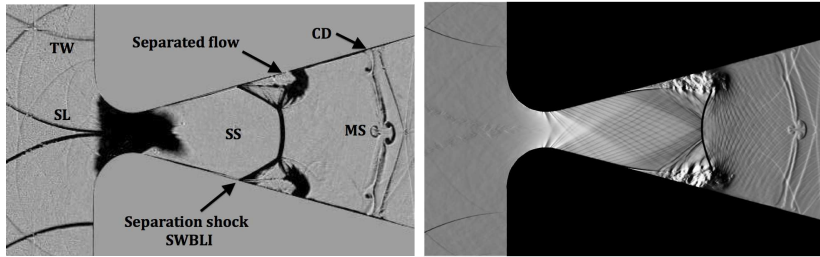


FIGURE 1. Comparison of the numerical and experimental Schlieren at $165\mu s$, mesh resolution: $98 \times 49 \times 196 \mu m^3$, MS: mushroom structure, CD: contact discontinuity, SS: secondary shock, SWBLI: shock wave boundary layer interaction, SL: slip line and TW: transverse wave (Results obtained in 2011).

al. [10] in a laboratory shock tube set-up. Amann, for instance, studied the influence of several parameters (nozzle half-angle, throat width and nozzle inlet radius) on the starting process of supersonic nozzles driven by a shock. Besides, special interest has been paid to the duration of the starting process, since it decreases the useful testing time of short-duration facilities. However, the evolution of the complex wave structures has also been shown.

From a numerical point of view, some studies were undertaken to simulate nozzle flow transients (startup and shutdown). Most of the simulations performed [11–13] were two-dimensional planar or axisymmetric, owing to the large amount of CPU time required for three-dimensional computations. Concerning rocket nozzles, Chen et al. [14] examined the flow structures of the start-up and shutdown processes using a Navier-Stokes solver. The configuration they studied was a sub-scale nozzle of a J-2S rocket engine (i.e. a precursor of the American Space Shuttle main engine). Also, Mouronval et al. [15, 16] studied numerically the early transient flow induced in an expanding nozzle by an incident planar shock wave and the appearance of a strong secondary shock wave. A detailed analysis of the wave structure was given and the mechanism of formation of vortices on the contact surface has been shown. Most of the previous studies dealt with the prediction of the main flow features (namely the primary and secondary shock waves, multiple shock wave reflections and slip surfaces). However, a detailed 3D investigation of transient shock/boundary layer interactions in such configurations has not been done so far.

The present work is a continuation of our previous investigation initiated during the 1st summer program held at the Technical University of Munich in 2011. Fig. 1 shows the comparison of the experimental and numerical Schlieren pictures from our previous attempt. It can be noted that the separation shock and the secondary shock structures were not fully captured in the numerical simulation. Nevertheless, a fairly good agreement was observed for the prediction of the primary and secondary shock speeds [17]. Here, we use again the LES to study the shock induced transient flow in a 3D planar nozzle (associated to a shock tube) with a larger spanwise domain size and increased mesh resolution. Particular emphasis has been made on the appearance of the secondary shock and its interaction with the boundary layer downstream of the throat region. Fundamentally, this study can be useful to strengthen the understanding of the shock-driven turbulence amplification associated with fast transient fluid flow. The quantification of interaction of turbulent fluctuations and its effect and mutual dependencies on overall dynamics of the complex flow evolution are important issues to deal with. The

report is organised as follows: A brief description of the numerical tools be presented in section 2. Section 3 illustrates the formulation of the numerical setup followed by the results and discussion in section 4. Finally, conclusions and future work are presented in section 5.

2. Numerical method

An in-house 3D compressible Navier-Stokes solver equipped with a fifth-order WENO scheme [19], WALE model [18] to handle the effect of the unresolved turbulent scales and an immersed boundary method [20–25] is used for the present simulations. The use of low-dissipation, high-order shock capturing schemes is an essential ingredient for computing complex compressible flows with shock waves. The diffusion terms are determined by means of fourth-order compact central difference formulas. The discretized equations are integrated in time by means of the explicit third-order total variation diminishing Runge-Kutta algorithm (RK3-TVD). The CFL number is set to 0.9 and a constant turbulent Prandtl number, $Pr_t = 0.9$ is used for all simulations. Detailed description of the applied methodology is reported in our previous works [17, 26, 27]. The simulations are performed on a SGI Altix ICE 8200EX and an IBM Power6 parallel computer of France.

3. Problem formulation

A shock wave with a prescribed shock Mach number (M_s) is allowed to pass through the nozzle situated at the end test section of the shock-tube arrangement. The Rankine-Hugoniot relations for a moving shock ($M_s = 1.86$) for air are used to set the left state (shocked gas, subscripted as '2') and right state (stagnant gas, subscripted as '1') of the shock wave. Geometric and flow parameters of the nozzle are: the radius of curvature of the nozzle converging section $R_n = 10$ mm, length of the nozzle $L_n = 142.871$ mm, nozzle angle = 15, throat length $L_t = 9.5$ mm, $p_1 = 98800$ Pa, $T_1 = 291.5$ K, $Re \approx 4.1 \times 10^5$ (based on L_t and properties at the left state). Although the experimental setup is having a cross-section of 80 mm×80 mm, the computational domain (lower half of the nozzle with symmetry condition) is chosen to have a $(40 \times L_t)$ mm² cross section. An immersed boundary technique is utilised to treat the nozzle boundaries within the Cartesian mesh. We used a reduced streamwise domain size of 160 mm (compared to the previous computational domain in [17]) and the leading edge of the nozzle is located at ≈ 56.5 mm. An isotropic mesh of size $\approx 49\mu\text{m}$ is prescribed and ≈ 343 Million fluid mesh points are chosen to resolve the flow domain. In order to compare computational data with experimental findings, the initial position of the shock wave is prescribed at the entrance of the nozzle. The bottom boundary is set to no-slip conditions while the spanwise direction (z-axis) is considered as periodic. Computations are stopped at $\approx 165\mu\text{s}$ with intermediate data saving at relevant time for comparison with the experimental counterpart (before the shock-wave reaches the left or right boundaries).

The initial turbulent flow fluctuations are assigned as homogeneous isotropic turbulent velocity fluctuations in the shocked gas region. A prescribed energy spectrum of Passot-Pouquet, $E(k^*) = A \left(\frac{k^*}{k_e^*} \right)^4 e^{-2 \left(\frac{k^*}{k_e^*} \right)^2}$ has been assumed to generate this initial velocity field. An open source [28] turbulent flow-field generator code has been used to get a box of turbulent fluctuations and this periodic data has been repeatedly assigned to fit into the computational domain of $160 \times 40 \times 9.5$ mm³. To generate a $(2\pi)^3$ box of

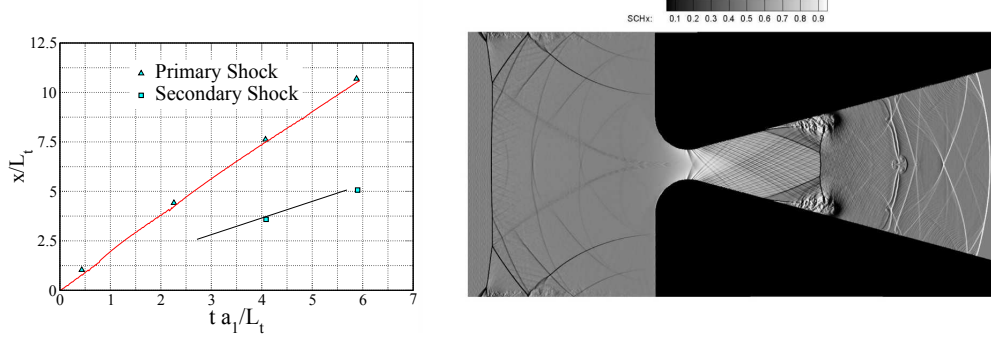


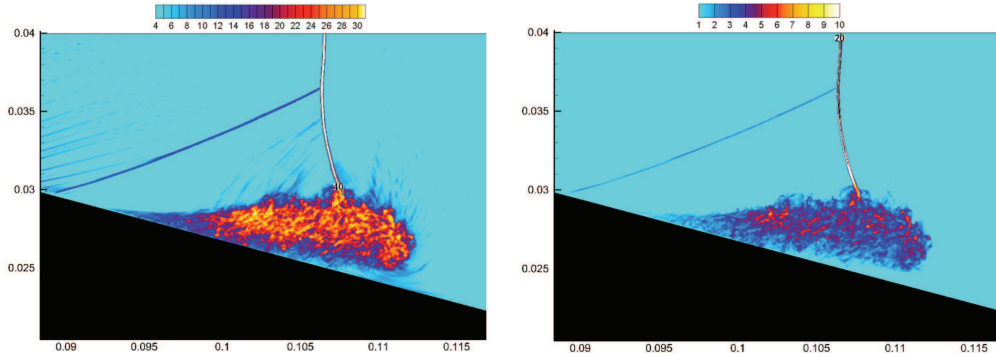
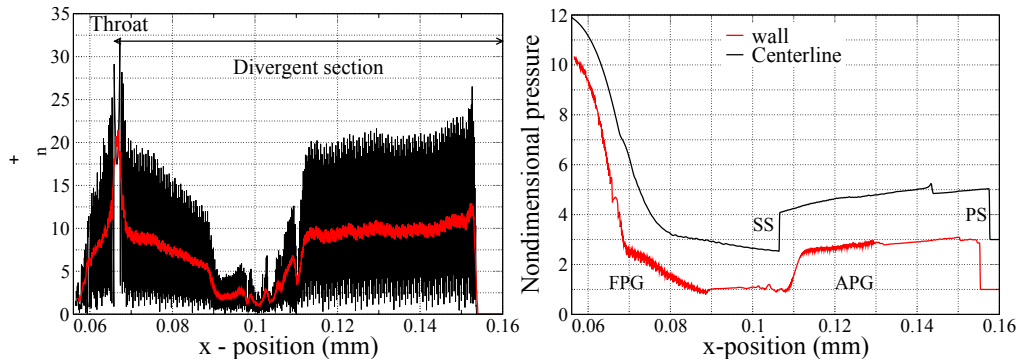
FIGURE 2. Evolution of shock position (symbols represent experimental data and solid lines are numerical results) and numerical Schlieren picture based on spatially averaged density at $\approx 165\mu s$ (New results).

turbulent fluctuations, the following parameters have to be chosen, i) Acoustic Reynolds number Re_{ac} , ii) non-dimensional turbulent velocity u_p^* and iii) most energetic length scale l_e^* . They are the same as described in our previous report [17]. An analysis of flow turbulence is presented on the basis of spatially averaged mean quantities over the homogeneous spanwise z-direction. Any averaged resolved quantity $\langle \tilde{\phi} \rangle$ is used to define a resolved fluctuating component $\tilde{\phi}'' = \tilde{\phi} - \langle \tilde{\phi} \rangle$.

4. Results and discussion

A part of the incident shock (IS) reflects and returns back upstream of the nozzle section as reflected shock (RS), while the part which entered into the nozzle, evolves as primary shock (PS) front, followed by a typical mushroom shaped contact surface (CS), while the boundary layer interaction with reflected transverse waves gives rise to a secondary shock (SS). It can be seen from Fig. 2 that the prediction of the primary and secondary shock speeds is in very good agreement with the experimental data. Numerical simulation at time $\approx 165\mu s$ is able to capture the shape of the separation shock, secondary shock, separation region and the finer structures associated with the mushroom structure (MS) of the contact discontinuity (compare also the experimental Schlieren picture Fig. 1).

The quality of the mesh and the LES model effectiveness can be assessed from the dissipation length scale and the sub-grid-scale viscosity estimation by the LES model. Fig. 3 is presented to substantiate the reliability of the mesh resolution for the present LES at time $\approx 165\mu s$. Kolmogorov scale is defined by $\eta = (\nu^3/\epsilon)^{1/4}$, where ϵ is the dissipation rate and ν is the kinematic viscosity. Following Pope [29] and assuming $\epsilon \approx \epsilon_{sgs} = C_E k_{sgs}^{3/2}/\Delta$, $k_{sgs} = (\nu_{sgs}/C_v \Delta)^2$, with $C_E = 0.7$, $C_v = 0.05$, the estimation of Δ/η can be obtained as a function of ν_{sgs} and model constants. It is argued in [29] that in an isotropic turbulence the maximum dissipation takes place at length scales of about 24η . As mentioned in [30, 31] at least two points are necessary to resolve any flow feature, a grid spacing of 12η is needed to resolve the scale of 24η . Inspecting the present outcome in Fig. (3) it can be concluded that the resolution is not too far from the acceptable limit of the required grid resolution for LES. The presence of shocks gives rise to higher values of both ν_{sgs}/ν and Δ/η in the vicinity of the shocks. The contours of the ratio of ν_{sgs}/ν shows the effectiveness of the WALE model in the vicinity of flow separation and


 FIGURE 3. Contour of Δ/η (left) and ν_{sgs}/ν (right).

 FIGURE 4. Δ_n^+ along the nozzle wall (left), wall pressure $\langle \bar{p}_w \rangle / p_1$ and centreline pressure $\langle \bar{p} \rangle / p_1$ (shifted by two units upwards).

in the shear layer region. From the spatially averaged mean flow quantities and the near wall fluid point co-ordinates (x,y) we obtain the near wall mesh resolution.

Fig. 4 shows that on an average (red curve generated by a running average of the black curve) $\Delta_n^+ < 10$ in the whole divergent section of the nozzle, and $\Delta_n^+ < 5$ near the flow separation region ($\Delta_n^+ = \Delta_n u_\tau / \nu_w$, where u_τ is the friction velocity, ν_w is the kinematic viscosity at the wall and Δ_n is the wall-normal distance of the near wall grid point). Nevertheless, near the throat region it reaches a higher value. The range of the values of Δ_n^+ can be considered as acceptable and as better agreeing with our previous [17] near wall resolution. The mean wall pressure reveals the flow regions associated with favourable pressure gradient (FPG) and adverse pressure gradient (APG) in the nozzle. Fig. 4 also shows the centreline pressure distribution depicting the location of PS and SS. The MS is clearly visible at the centreline density profile (Fig. 5). Its Mach number reaches a maximum value of ≈ 2.7 in the divergent section and reduces to ≈ 1.2 after the SS, relaxing to sonic and subsonic levels subsequently and being linked with the PS. The wall shear stress illustrates the flow separation region and flow reattachment. A smaller separation bubble is clearly visible along with the main separation bubble in Fig. 5. An enlarged mean flow-field is depicted in Fig. 6. The streamlines and velocity vectors corroborate with the location of separation bubbles and the subsequent flow reattachment represented by zero wall shear stress.

The 3D turbulent flow structures are visualised by plotting the positive iso-surfaces of the second invariant of the velocity gradient tensor Q , defined as $Q = 0.5(\Omega_{ij}\Omega_{ij} - S_{ij}S_{ij})$,

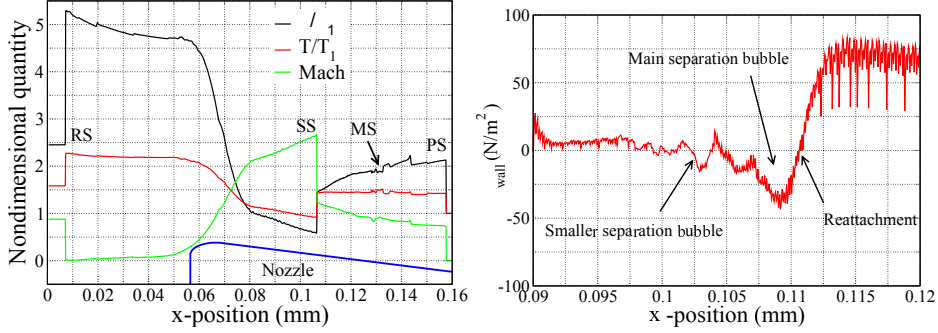
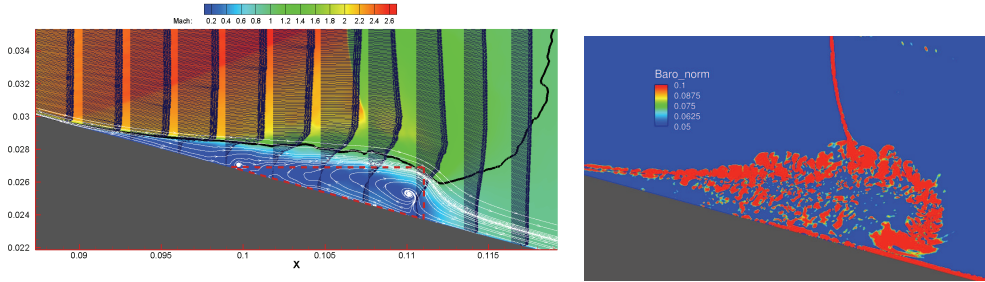


FIGURE 5. Centreline mean flow properties (left) and wall shear stress (right).

FIGURE 6. Mean flow visualisation, black solid curve represents the sonic line (left), Contours of the baroclinic torque term $|\nabla\rho \times \nabla p|L_t^2/(p_2\rho_2)$ (right).

where, $S_{ij} = 0.5(u_{i,j} + u_{j,i})$ and $\Omega_{ij} = 0.5(u_{i,j} - u_{j,i})$ following the usual notation. Vortex convection and stretching are essentially nonlinear mechanisms through which fine-scale and intense vorticity fluctuations are generated and maintained. It can be emphasised that the baroclinic torque term due to non-collinear ∇T and ∇S , in other words $\nabla\rho \times \nabla p \neq 0$ are expected to contribute to the production of vorticity in the vicinity of the SS interaction with the separated flow (see Fig. 6). Vortical structures shown in Fig. 7, reveal the characteristics of compressible turbulent shear layers depicting deformed, stretched, coiled and elongated vortex tubes in the streamwise, transverse and spanwise directions. The present LES has captured the larger and smaller turbulent structures associated with flow separation and the shear layer region interacting with the SS.

Instantaneous flow data and spatially averaged mean quantities are extracted from the region marked in red (data window shown in Fig. 6). They are used to analyse the spatial structures at $165\mu s$. Fig. 7 also illustrates the PDF of standardised instantaneous quantities (vorticities & spatial derivatives of velocity components). The flatness values of these lie in the range of 6-12 indicating the similar properties of the double-exponential or exponential distribution of the PDF with nonzero low skewness values. On the other hand, the PDF of fluctuating velocity components assumes flatness values ≈ 5 with non-zero skewed distributions compared to a Gaussian distribution (Fig. 8). The two-point autocorrelation coefficients for (Fig. 8 right) fluctuating velocity components (at $y=0.026$ mm) within this data window are computed to evaluate the effect of spanwise domain size on the turbulence. It is clear from this figure that the autocorrelation coefficients reduces to zero within half of the spanwise domain size, so that the domain is sufficiently large to enforce periodic boundary conditions without inhibiting the turbulence. The re-

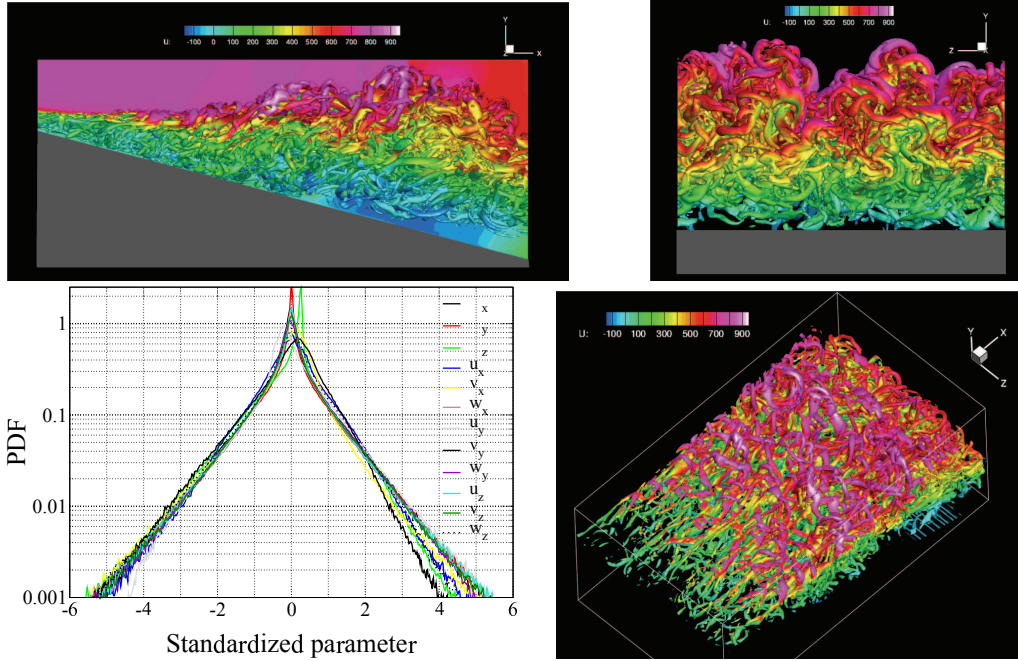


FIGURE 7. 3D flow visualisation by iso-surfaces of Q , flooded with streamwise velocity contours. Shown are the PDFs of instantaneous vorticity components and velocity gradients.

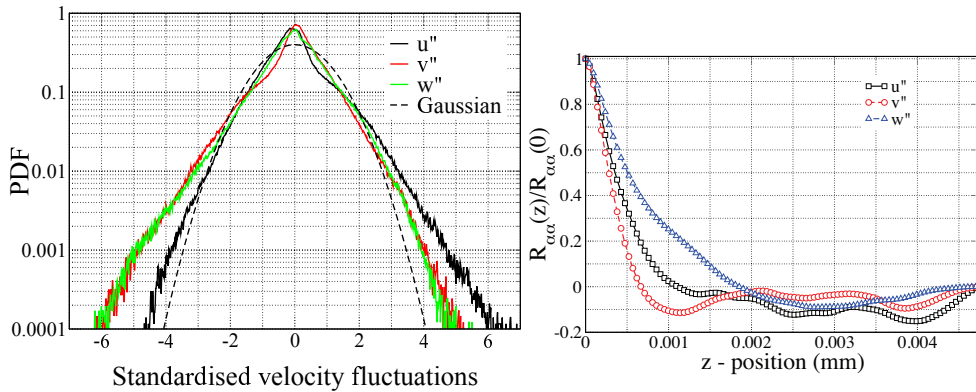


FIGURE 8. Standardised PDF of fluctuating components (left), two-point correlation of fluctuation components (right).

solved Reynolds stress terms reveal the prevailing anisotropy (Fig. 9) in the interaction region. As expected, the dominant terms are R_{11} , R_{22} , R_{33} and R_{12} . The estimated turbulent kinetic energy (Fig. 10) attains a maximum value of $\approx 47\%$ of the kinetic energy of the initial left state, indicating high turbulent intensity in the upper section of the compressible shear layer region. The scatter plots (Fig. 10) of fluctuating components of the velocity field (within the data window) seem to show an anti correlation between streamwise and transverse components. Other combinations appeared as without any preferential correlation.

We are aware of the fact that the extraction of fluctuating components based on only

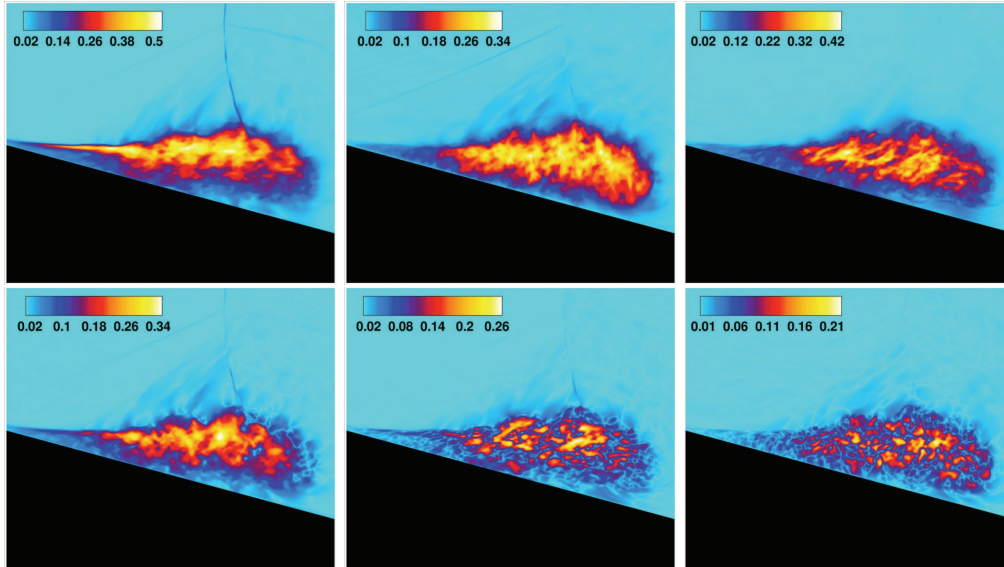


FIGURE 9. Resolved Reynolds stress $\sqrt{\bar{R}_{ij}}/U_2$ where, $R_{ij} = \frac{\langle \bar{\rho} \overline{u'_i u'_j} \rangle}{\langle \bar{\rho} \rangle}$, top: R_{11} , R_{22} & R_{33} (left to right) and bottom: R_{12} , R_{13} & R_{23} (left to right).

spatially averaged mean quantities suffers from insufficient stability of mean flow variables. We attempted to add temporal filtering to spanwise ensemble averaging, as an initial trial. A suitable filter length had to be estimated without affecting the unsteadiness of the flow for this purpose. The convective time scales associated with the speed of the dominant shocks (PS, SS) or the initial left state velocity together with the mesh size were used to define temporal filter lengths. The linear approximation of shock speeds from experimental findings yields Mach numbers of PS and SS as $M_{ps} \approx 1.8$ and $M_{ss} \approx 0.66$ respectively. Three test runs were carried out utilising multiples of the filter length $\tau_f = \Delta/(a_1 M_{ss})$, where Δ is the minimum mesh size ($49\mu\text{m}$). It can be seen from Fig. 11 that the applied time filter produces deviations of the flow separation bubble, affecting the mean flow-field. This problem could perhaps be cured by post-processing the flow data and including symmetric temporal filtering stencils at the corresponding instants of time. An alternative, to be tested in the future, would be ensemble-averaging of a number of flow realisations, obtained by slightly modifying the phases of the initial turbulent fields [32].

An estimation of four budget terms of the turbulent kinetic energy based on spatially averaged quantities are shown in Fig. 12. This rough estimation reveals that the turbulent kinetic energy production, turbulent transport and pressure dilatation terms are dominant for the non-equilibrium turbulent state. The plot of the pressure dilatation terms also shows fairly high positive and negative values (red and blue regions). However, they appear immediately downstream of the SS and not in the shear layer. It can be noted that the sporadic patches (dark blue region) of negative production of turbulent kinetic energy are predicted. This can be associated to density changes (shear layer subjected to compressions/expansions [33, 34]) in this region and strongly out of equilibrium behaviour of the turbulent flow can exist during the transient flow development. We are aware of the fact that the dissipation term can not be reliably predicted in an LES. Nev-

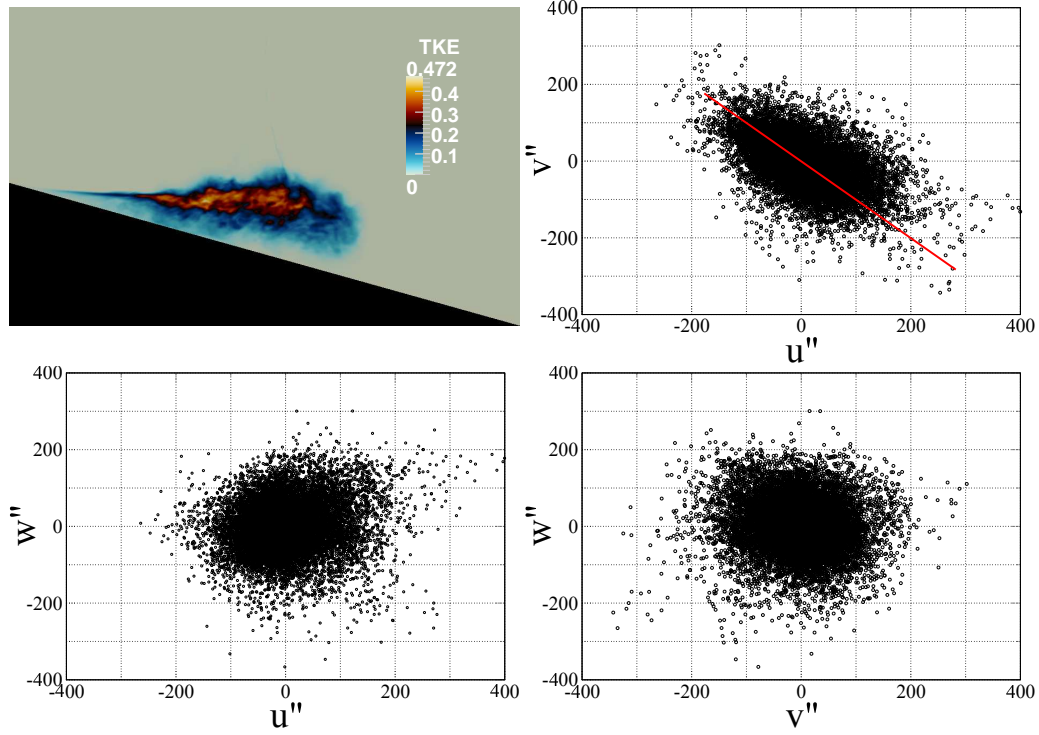


FIGURE 10. Turbulent kinetic energy $k/0.5U_2^2$ and scatter plots of the fluctuating velocity components.

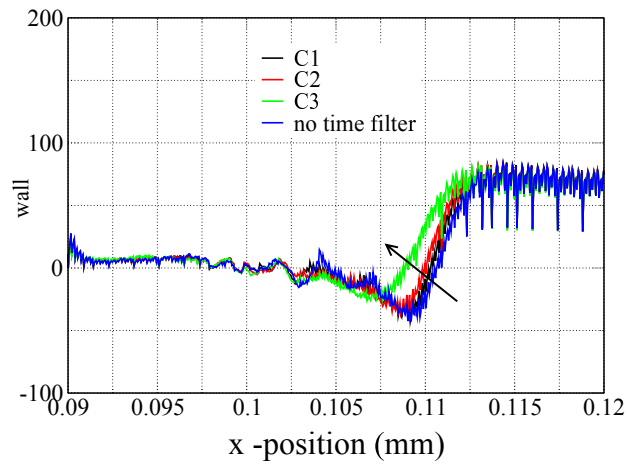


FIGURE 11. Wall shear stress for various time filter width, C1 : $10\tau_f$, C2 : $20\tau_f$ and C3 : $50\tau_f$.

ertheless, it provides some interesting insight. A deeper and more reliable analysis of the turbulent budget terms will be made in our future study adopting phase averaging with more stable statistics.

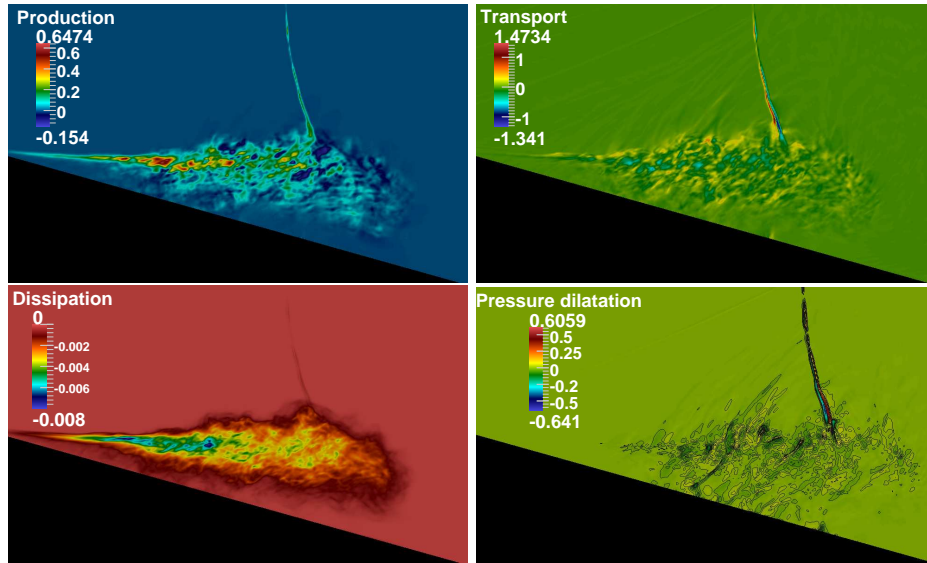


FIGURE 12. Turbulent budget terms: i) Production (top left), ii) Transport (top right), iii) Dissipation (bottom left), iv) Pressure dilatation: black contour lines are values between -0.1 and 0.1 (bottom right), all terms are non-dimensionalised by $U_2^3 \rho_2 / L_t$.

5. Conclusions

In this work, LES is carried out to resolve numerically the complex flow features associated with shock induced supersonic flow inside a planar nozzle in a shock-tube arrangement. A numerical flow solver equipped with a high-order WENO scheme and an immersed boundary technique is utilised. The global flow features of primary, secondary shock waves and contact discontinuity are well captured and in good agreement with the experimental data. The lack of information of the initial level of turbulence in the experiments leads to the difficulties involved in the proper choice of the initial flow-field and the assumption of initial turbulent parameters. Homogeneous isotropic turbulent flow fluctuations are superimposed onto the shocked left state as initial fluctuating flow-field. Larger spanwise domain size (one throat length) and higher mesh resolution (isotropic mesh size of $49\mu\text{m}$) are used to simulate the transient nozzle flow. A symmetry condition on the mid-plane and a reduced streamwise domain size are used compared to the previous study, in order to allow for an increased resolution, where it is needed. A preliminary analysis of the flow physics is made based on mean properties (ensemble averaged in spanwise direction) and a comparison with previous results and experimental data promises reliability. However, the computation of turbulence statistics (Reynolds stresses etc.), needs more stable (mean) flow variables. An attempt with extra temporal averaging during the simulation found to be inadequate, because the temporal filters are biased to the past information without any future information while calculating on the fly. To achieve stable statistics, further ensemble averaging has to be performed, based on 5-10 more simulations with little phase-incoherence in the free-stream isotropic turbulence. Physically meaningful fluctuations can thereby be received which are needed to compute correlations. Future work has to address this, before effects of flow acceleration on the mixing layer (which surrounds the separation bubble), of the dynamics of

the separation bubble and of the shock unsteadiness can be investigated in a deeper analysis.

Acknowledgments

The authors gratefully acknowledge the financial support provided by the German Research Foundation (Deutsche Forschungsgemeinschaft – DFG) in the framework of the Sonderforschungsbereich/Transregio 40 and the IGSSE (International Graduate School of Science and Engineering) at the TU München. We have utilized the computational facilities from GENCI [CCRT/CINES/IDRIS] (grant 2010-0211640) and Leibniz-Rechenzentrum München (LRZ). Authors are also grateful to Prof. G. Ben-Dor and Dr. O. Sadot (Ben-Gurion University), for providing some of their experimental results. Special thanks go to Prof. F. Hussain (Texas Tech. University) and Prof. T. Gatski (University of Poitiers) for their insightful comments and suggestions throughout this project. We also acknowledge the support from all members of the in-house code *ChocWaves* developers.

References

- [1] HAGEMANN, G. AND FREY, M. (2008). Shock pattern in the plume of rocket nozzles: needs for design consideration. *Shock Waves*, **17**, 387–395.
- [2] SHIMIZU, T. AND NOBUHIRO, Y. (2003). Numerical simulation of rocket engine internal flows. *Annual report of the Earth Simulator Centre*, 133–136, April 2002–March 2003.
- [3] WANG, T.-S. (2005). Transient three-dimensional analysis of nozzle side load in regeneratively cooled engines. *AIAA 2005-3942*.
- [4] GROSS, A. AND WEILAND, C. (2004). Numerical simulation of separated cold gas nozzle flows. *Propulsion & Power*, **20**(3), 509–519.
- [5] GROSS, A. AND WEILAND, C. (2004). Numerical simulation of hot gas nozzle flows. *J. Propulsion & Power*, **20**(5), 879–891.
- [6] OSTLUND, J. (2004). Supersonic flow separation with application to rocket engine nozzles. *Technical reports from Royal Institute of Technology*, Dept. of Mechanics.
- [7] SHIMIZU, T., KODERA, M. AND TSUBOI, N. (2008). Internal and external flow of rocket nozzle. *J. of the earth Simulator*, **9**, 19–26.
- [8] SMITH, C. E. (1966). The starting process in a hypersonic nozzle. *J. Fluid Mechanics*, **24**, 625–640.
- [9] AMANN, H. O. (1967). Experimental study of the starting process in a reflection nozzle. *Phys. Fluids*, 150–153.
- [10] SAITO, T. AND TAKAYAMA, K. (1999). Numerical simulations of nozzle starting process. *Shock Waves*, **9**, 73–79.
- [11] TOKARCIC-POLSKY, S. AND CAMBIER, J. L. (1994). Numerical study of transient flow phenomena in shock tunnels. *AIAA J.*, **32**(5), 971–978.
- [12] PRODROMOU P. AND HILLIER R. (1992). Computation of unsteady nozzle flows. *In the proceedings of the 18th ISSW, Sendai, Japan*, **II**, 1113–1118.
- [13] IGRA, O., WANG, L., FALCOVITZ, J. AND AMANN, O. (1998). Simulations of the starting flow in a wedge-like nozzle. *Shock Waves*, **8**, 235–242.
- [14] CHEN C. L., CHAKRAVARTY, S. L. AND HUNG C. M. (1994). Numerical Investigation of Separated Nozzle Flows. *AIAA J.*, **32**, 1836–1843.
- [15] MOURONVAL, A. S., HADJADJ, A., KUDRYAVTSEV, A. N. AND VANDROMME, D. (2002). Numerical investigation of transient nozzle flow. *Shock Waves*, **12**, 403–411.

- [16] MOURONVAL, A. S. AND HADJADJ, A. (2005). Numerical study of starting process in a supersonic nozzle. *J. Propulsion & Power*, **21**(2), 374–378.
- [17] CHAUDHURI, A., HADJADJ, A., GATSKI, T. AND FRIEDRICH, R. (2011). Large-eddy simulation of shock/boundary layer interaction in transient nozzle flows. *SFB/TRR 40 – Proceedings of the Summer Program 2011*.
- [18] NICOUD, F. AND DUCROS, F. (1999). Subgrid-scale stress modelling based on the square of the velocity gradient tensor. *Flow, Turbulence and Combustion*, **62**, 183–200.
- [19] JIANG, G. AND SHU, C. W. (1996). Efficient implementation of weighted ENO schemes. *J. Comp. Phys.*, **126**, 202–228.
- [20] PESKIN, C. S. (1972). *Flow patterns around heart valves: a digital computer method for solving the equations of motion*. Ph.D. thesis, Albert Einstein Coll. Med.
- [21] MITTAL, R. AND IACCARINO, G. (2005). Immersed boundary methods. *Ann. Rev. Fluid Mech.*, **37**, 239–261.
- [22] IACCARINO, G. AND VERZICCO, R. (2003). Immersed boundary technique for turbulent flow simulations. *Appl. Mech. Rev.*, **56**, 331–347.
- [23] TSENG, Y. AND FERZIGER, J. H. (2003). A ghost-cell immersed boundary method for flow in complex geometry. *J. Comp. Phys.*, **192**, 593–623.
- [24] GAO, T., TSENG, Y. AND LU, X. (2007). An improved hybrid cartesian/immersed boundary method for fluid-solid flows. *Int. J. Numer. Meth. Fluids*, **55**, 1189–1211.
- [25] DADONE, A. AND GROSSMAN, B. (2004). Ghost-cell method for inviscid two-dimensional flows on cartesian grids. *AIAA J.*, **42**(12), 2499–2507.
- [26] CHAUDHURI, A., HADJADJ, A. AND CHINNAYYA, A. (2011). On the use of immersed boundary methods for shock/obstacle interactions. *J. Comp. Phys.*, **230**, 1731–1748.
- [27] CHAUDHURI, A., HADJADJ, A., CHINNAYYA, A. AND PALERM, S. (2011). Numerical study of compressible mixing layers using high-order WENO schemes. *J. Sci. Computing*, **47**(2), 170–197.
- [28] TH3DR8 (SOURCE CODE), Generation of incompressible 3D homogeneous isotropic turbulence. Available at <http://www.cerfacs.fr>.
- [29] POPE, S. B. (2000). *Turbulent flows*. Cambridge university press, Cambridge.
- [30] FRÖHLICH, J., MELLEN, C. P., RODI, W., TEMMERMAN, L. AND LESCHZINER, M. A. (2005). Highly resolved large-eddy simulation of separated flow in a channel with streamwise periodic constrictions. *JFM*, **526**, 19–66.
- [31] CAVAR, D. AND MEYER, K. E. (2012). LES of turbulent jet in cross-flow: Part 1 - A numerical validation study. *IJHFF*, **36**, 18–34.
- [32] HUSSAIN, A. K. M. F. (1986). Coherent structures and turbulence. *JFM*, **173**, 303–356.
- [33] GAVIGLIO, J., DUSSAUGE, J. P., DEBIEVE, J. F. AND FAVRE, A. (1977). Behavior of a turbulent flow, strongly out of equilibrium, at supersonic speeds. *Phys. Fluids*, **20**, S179.
- [34] DUSSAUGE, J. P., GAVIGLIO, J. AND FAVRE, A. (1978). Density changes and turbulence production in the expansion or compression of a turbulent flow at supersonic speed. *Lecture Notes in Physics*, **76**, 385–395.